fcc phase, the final Pt-Ni octahedra after 42 hours of growth exhibited asymmetric diffraction peaks, implying the coexistence of a Pt-richer phase and a Ni-richer phase.

To demonstrate the general importance of the element-specific anisotropic growth mechanism, we further synthesized Pt-Co NCs by replacing $Ni(acac)_2$ with $Co(acac)_2$ while keeping all other conditions unchanged. After 42 hours of reaction time, octahedral $PtCo_{1.5}$ NCs were successfully prepared. By following their morphological and compositional evolution after different growth times (fig. S7), we observed a growth trajectory of the $PtCo_{1.5}$ octahedra similar to that of the $PtNi_{1.5}$ octahedra. The growth of Pt-rich hexapods/concave octahedra before the final formation of Co-rich octahedra again suggests a delayed anisotropic deposition of a Co-rich phase at the concave {111} surfaces. Thus, the element-specific anisotropic growth appears to be an important mechanism for the formation of a variety of shaped Pt alloy NCs in solution-phase co-reduction.

Figure 4E presents a comprehensive, atomic-scale "life-cycle" model of our bimetallic nano-octahedra, including their unusual anisotropic growth pathway and their previously reported degradation pathway during acidic ORR electrocatalysis (*22*). Our results reveal a previously overlooked element-specific, compositionally anisotropic growth mechanism of shaped Pt alloy NCs, where rapid growth of Pt-rich hexapods/concave octahedra along ⟨100⟩ directions precedes delayed deposition of Ni-rich phase at the concave {111} sites. Whereas the growth of Pt-rich hexapods is a ligand-controlled kinetic process, the step-induced deposition of the Ni-rich phase at the concave surface resembles a thermodynamically controlled process accomplished in a much longer time. The element-specific anisotropic growth provides the origin of our previously reported compositional segregation (Ni-rich facets and Pt-rich corners/edges) and chemical degradation pathway of the Pt-Ni octahedra (*22*), which underwent a selective etching of the Ni-rich {111} facets and thus activity instability during the ORR electrocatalysis in acidic electrolyte (Fig. 4E and fig. S8). While forming a catalytically active Pt-rich shell, the selective etching of the Ni-rich {111} facets resulted in concave octahedra with the exposure of less active facets such as {100} and {110}. Extended potential cycling further resulted in the re-emergence of Pt-rich hexapods and almost none of the catalytically active {111} surfaces survived, leading to substantial activity degradation. Evidently, the fate of the shaped Pt bimetallic NCs during long-term ORR electrocatalysis is substantially determined by the early stages of their element-specific aniso tropic growth during synthesis.

Our results highlight the importance of understanding the element-by-element growth mechanism of shaped alloy NCs. The possibility of controlling the element-specific anisotropic growth modes of such NCs may enable the rational synthesis of Pt alloy nano-octahedra ORR electrocatalysts with desired surface composition (e.g., Pt-richer {111} facets) and sustained high activity.

REFERENCES AND NOTES

1. T. S. Ahmadi, Z. L. Wang, T. C. Green, A. Henglein, M. A. El-Sayed, *Science* **272**, 1924–1926 (1996).
2. N. Tian, Z.-Y. Zhou, S.-G. Sun, Y. Ding, Z. L. Wang, *Science* **316**, 732–735 (2007).
3. H. A. Gasteiger, N. M. Marković, *Science* **324**, 48–49 (2009).
4. V. R. Stamenkovic *et al*., *Science* **315**, 493–497 (2007).
5. M. K. Debe, *Nature* **486**, 43–51 (2012).
6. G. Wu, K. L. More, C. M. Johnston, P. Zelenay, *Science* **332**, 443–447 (2011).
7. D. Xu *et al*., *Angew. Chem. Int. Ed.* **48**, 4217–4221 (2009).
8. J. Zhang, J. Fang, *J. Am. Chem. Soc.* **131**, 18543–18547 (2009).
9. J. Zhang, H. Yang, J. Fang, S. Zou, *Nano Lett.* **10**, 638–644 (2010).
10. J. Wu, A. Gross, H. Yang, *Nano Lett.* **11**, 798–802 (2011).
11. M. K. Carpenter, T. E. Moylan, R. S. Kukreja, M. H. Atwan, M. M. Tessema, *J. Am. Chem. Soc.* **134**, 8535–8542 (2012).
12. C. Cui *et al*., *Nano Lett.* **12**, 5885–5889 (2012).
13. Y. Wu, S. Cai, D. Wang, W. He, Y. Li, *J. Am. Chem. Soc.* **134**, 8975–8981 (2012).
14. S.-I. Choi *et al*., *Nano Lett.* **13**, 3420–3425 (2013).
15. J. Wu *et al*., *J. Am. Chem. Soc.* **134**, 11880–11883 (2012).
16. H. Zhang *et al*., *J. Am. Chem. Soc.* **133**, 6078–6089 (2011).
17. Y. Wu *et al*., *Angew. Chem. Int. Ed.* **51**, 12524–12528 (2012).
18. X. Liu *et al*., *Sci. Rep.* **3**, 1404 (2013).
19. E. Christoffersen, P. Liu, A. Ruban, H. L. Skriver, J. K. Norskov, *J. Catal.* **199**, 123–131 (2001).
20. G. Wang, M. A. Van Hove, P. N. Ross, M. I. Baskes, *J. Chem. Phys.* **122**, 024706 (2005).
21. I. A. Abrikosov, A. V. Ruban, H. L. Skriver, B. Johansson, *Phys. Rev. B* **50**, 2039–2042 (1994).
22. C. Cui, L. Gan, M. Heggen, S. Rudi, P. Strasser, *Nat. Mater.* **12**, 765–771 (2013).
23. C. Chen *et al*., *Science* **343**, 1339–1343 (2014).
24. J. M. Petroski, Z. L. Wang, T. C. Green, M. A. El-Sayed, *J. Phys. Chem. B* **102**, 3316–3320 (1998).
25. T. Yu, Y. Kim, H. Zhang, Y. Xia, *Angew. Chem. Int. Ed.* **50**, 2773–2777 (2011).
26. H. Zheng *et al*., *Science* **324**, 1309–1312 (2009).
27. J. M. Yuk *et al*., *Science* **336**, 61–64 (2012).
28. H.-G. Liao, H. Zheng, *J. Am. Chem. Soc.* **135**, 5038–5043 (2013).
29. H.-G. Liao, L. Cui, S. Whitelam, H. Zheng, *Science* **336**, 1011–1014 (2012).
30. Y. Xia, Y. Xiong, B. Lim, S. E. Skrabalak, *Angew. Chem. Int. Ed.* **48**, 60–103 (2009).
31. Y. Wu *et al*., *J. Am. Chem. Soc.* **135**, 12220–12223 (2013).
32. Y. Ding, F. Fan, Z. Tian, Z. L. Wang, *J. Am. Chem. Soc.* **132**, 12480–12486 (2010).

ACKNOWLEDGMENTS

Supported by U.S. Department of Energy EERE award DE-EE0000458 via subcontract through General Motors; the Ernst Ruska Center for Microscopy and Spectroscopy with Electrons, Forschungszentrum Jülich GmbH, Germany; and Deutsche Forschungsgemeinschaft (DFG) grants STR 596/4-1 ("Pt stability") and STR 596/5-1 ("Shaped Pt bimetallics"). We thank the Zentraleinrichtung für Elektronenmikroskopie (Zelmi), Technical University Berlin, for its support of TEM and EDX measurements; N. Erini for carrying out FTIR measurements; and R. Schomack and M. Gleich for analysis of thermal gravimetric data.

SUPPLEMENTARY MATERIALS

www.sciencemag.org/content/346/6216/1502/suppl/DC1
Materials and Methods
Figs. S1 to S8
References (*33*, *34*)

15 September 2014; accepted 19 November 2014
10.1126/science.1261212

EARTH MAGNETOSPHERE

Direct observation of closed magnetic flux trapped in the high-latitude magnetosphere

R. C. Fear,[1*†] S. E. Milan,[1,2] R. Maggiolo,[3] A. N. Fazakerley,[4] I. Dandouras,[5,6] S. B. Mende[7]

The structure of Earth's magnetosphere is poorly understood when the interplanetary magnetic field is northward. Under this condition, uncharacteristically energetic plasma is observed in the magnetotail lobes, which is not expected in the textbook model of the magnetosphere. Using satellite observations, we show that these lobe plasma signatures occur on high-latitude magnetic field lines that have been closed by the fundamental plasma process of magnetic reconnection. Previously, it has been suggested that closed flux can become trapped in the lobe and that this plasma-trapping process could explain another poorly understood phenomenon: the presence of auroras at extremely high latitudes, called transpolar arcs. Observations of the aurora at the same time as the lobe plasma signatures reveal the presence of a transpolar arc. The excellent correspondence between the transpolar arc and the trapped closed flux at high altitudes provides very strong evidence of the trapping mechanism as the cause of transpolar arcs.

The night side of the terrestrial magnetosphere forms a structured magnetotail, consisting of a plasma sheet at low latitudes that is sandwiched between two regions called the magnetotail lobes (Fig. 1). The lobes consist of the regions in which the terrestrial magnetic field lines are directly connected to the interplanetary magnetic field (IMF), which is referred to as being topologically "open" (indicated by the dashed gray lines in Fig. 1). Magnetic field lines threading the plasma sheet (solid gray lines in Fig. 1) are not connected to the IMF and are therefore "closed" (*1*, *2*). Topology changes are caused by the process of magnetic reconnection, which drives magnetospheric dynamics when the IMF is southward (*1*).

Different plasma populations are observed in these regions: Plasma in the lobes is very cool, whereas the plasma sheet is more energetic. The key way to distinguish between open and closed magnetic field lines is that electron distributions on closed field lines may exhibit a double loss cone, in which the distribution peaks perpendicular to the magnetic field (*3*). This requires the presence of magnetic mirrors on both sides of the observation site; therefore, double loss cones are unambiguous indicators that the magnetic field lines observed by a spacecraft are closed.

A major problem in magnetospheric physics is the adaptation of this picture to times when the IMF is northward. In a recent study (*4*), Shi *et al.* have reported relatively hot plasma in the lobes, which is unexpected in standard magnetosphere model. The authors attributed the presence of the plasma to direct entry of the solar wind, implying that it should be observed on open magnetic field lines. However, similar observations (*5*, *6*) have previously been interpreted as spatially separated filaments protruding from the plasma sheet into the lobe [though Huang *et al.* noted that no theoretical description existed to explain their presence (*6*)]. In these studies, the observed plasma has been isotropic, but different magnetic field topologies and interpretations have been inferred due to the absence of evidence of a loss cone.

Another controversy concerns the cause of an auroral configuration called the transpolar arc, which occurs at very high latitudes when the IMF is northward (*7*, *8*). There is no consensus on whether transpolar arcs occur on field lines that are closed (*3*, *7*–*10*) or open (*11*–*13*). Their formation remains the subject of debate, with a range of competing theories (*14*–*20*). One mechanism for transpolar arcs is for them to result from the closure of lobe magnetic flux, which then remains trapped in the magnetotail (*10*); this hypothesis makes a number of predictions that have recently been validated statistically (*14*, *20*). If this is true, a spacecraft situated in the lobe should observe a wedge of closed flux sandwiched within the lobe at high latitudes, well away from the expected location of the plasma sheet.

Virtually all plasma observations of transpolar arcs have come from spacecraft at low altitudes; these observations therefore report the precipitation associated with the arc rather than a direct measurement of the source plasma for the arc. It has been argued that further examination of in situ observations in the lobes (i.e., at much higher altitudes) is necessary to identify the source plasma and the processes causing transpolar arcs (*8*). To date, only one study has reported such observations (*6*), which revealed relatively hot plasma, similar to the atypically hot lobe plasma signatures discussed above (*4*, *5*). The authors concluded that they detected the source plasma for a transpolar arc but that the observed structures were not explained by any existing theory. Here we demonstrate that the presence of this plasma can be explained by the trapped flux mechanism for the formation of transpolar arcs (*10*) by showing that a double loss cone is observed within the plasma and that the plasma observations correspond extremely well to the back-and-forth motion of a transpolar arc.

On 15 September 2005, the Cluster 1 spacecraft was situated in the southern hemisphere lobe (Fig. 1). An overview of the IMF and the observations made by Cluster 1 is shown as a function of time in Fig. 2. The main period of interest is between 16:00 and 19:00 UT, when the IMF was northward (indicated by a north-south component $B_Z > 0$) (Fig. 2A). Before 17:00 and after 19:00 UT, the ions observed were cool (<500 eV) (Fig. 2D), which is consistent with upwelling from the ionosphere and typical of the lobe. However, between 17:00 and 19:00 UT, a much more energetic plasma population was observed (~1-keV electrons and ~10-keV ions) (Fig. 2, C and D), which is comparable to the mean plasma sheet energy when the IMF is northward (*21*). The electron and ion energies and temperatures (Fig. 2, C to E) are comparable to those reported in previous studies (*4*–*6*).

The electron pitch angles observed between 18:15 and 18:45 UT are plotted in Fig. 3A. Cluster 1 observed bidirectional electrons (peaking at pitch angles of 0° and 180°) throughout the interval, except at ~18:36 UT when the electron distribution was not only more intense but also peaked at pitch angles nearer 90°. Figure 3B shows the pitch angle distribution averaged over 21 s centered on 18:36:43 UT (indicated as "g" in Fig. 3A). The color scale has been selected to emphasize the variations between different pitch angles. The parallel and antiparallel fluxes were approximately half the value observed perpendicular to the magnetic field. This double loss cone is extremely strong evidence that the plasma observed by Cluster was on closed magnetic field lines. The bidirectional electrons observed beforehand (between 18:15 and 18:35 UT) are also consistent with electrons observed on closed magnetic field lines—in typical magnetotail crossings, bidirectional electrons are observed through much of the outer plasma sheet, with double loss cone distributions deep in the central plasma sheet (*21*). Ion distributions observed at this time are indicative of the occurrence of magnetotail reconnection tailward of the spacecraft (fig. S1).

Simultaneous observations of the Southern Hemisphere aurora on a global scale are available for this period from the far ultraviolet (FUV) Wideband Imaging Camera (*22*) on the IMAGE (Imager for Magnetopause-to-Aurora Global Exploration) satellite (Fig. 4A). (The location of IMAGE is also indicated in Fig. 1, and the full sequence of auroral images is shown in movie S1.) In Fig. 4A, the location of Cluster 1 has been mapped onto the Southern Hemisphere ionosphere along the model magnetic field lines (*23*) of Fig. 2. There is an excellent match between the plasma observations made by Cluster and the location of the transpolar arc relative to the footprint of the spacecraft (see Fig. 2 and movie S1). The second time that the arc intersects the spacecraft footprint [Fig. 4A, panel (g)] corresponds with the time that the highest intensities of energetic plasma were observed by Cluster, which is when the double loss cone was observed in Fig. 3B.

Our observations demonstrate that atypically hot plasma observed in the lobe occurs on closed magnetic field lines and is therefore incompatible with direct entry from the solar wind. The excellent match between the plasma observations and the intersections of the transpolar arc and the spacecraft footprints (d, f, and g in Figs. 2 and 4) confirms that such atypically hot plasma is the source plasma for transpolar arcs. The correspondence between the intersections of the arc and the observation of hotter plasma at two distinct times also demonstrates that the cause of multiple sequential observations of such atypical plasma is the back-and-forth motion of the closed magnetic field lines; that is, they are not necessarily spatially separated filaments, as previously

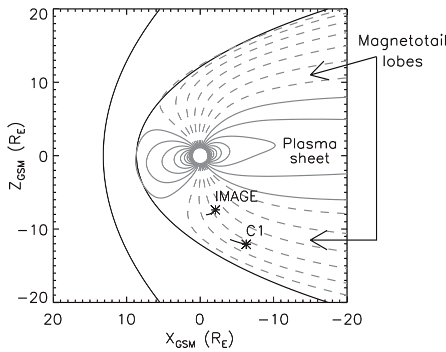

Fig. 1. Locations of the Cluster 1 and IMAGE spacecraft between 17:00 and 19:00 UT on 15 September 2005. Positions are projected into the *xz* plane of the Geocentric Solar Magnetic (GSM) coordinate system (*24*), in which the *x* axis is directed toward the Sun and the *z* axis is toward magnetic north. Asterisks denote spacecraft locations at 17:00 UT (C1 indicates Cluster 1). Solid black lines indicate model locations for the bow shock and magnetopause; gray lines indicate model geomagnetic field lines from an empirical model (*23*). The field lines that are expected to be closed are plotted as solid lines, whereas those that would normally be open—and hence connected to the solar wind downtail—are dashed. Cluster 1 was deep inside the lobe, a long way from the expected location of the closed field line region (the plasma sheet). 1 R_E is one Earth radius (6400 km).

[1]Department of Physics and Astronomy, University of Leicester, Leicester, UK. [2]Birkeland Centre for Space Sciences, University of Bergen, Bergen, Norway. [3]Belgian Institute for Space Aeronomy, Brussels, Belgium. [4]Mullard Space Science Laboratory, University College London, Dorking, UK. [5]Institut de Recherche en Astrophysique et Planétologie (IRAP), UMR 5277, Université Paul Sabatier–Observatoire Midi-Pyrénées, University of Toulouse, Toulouse, France. [6]IRAP, CNRS, Toulouse, France. [7]Space Sciences Laboratory, University of California Berkeley, Berkeley, CA 94720, USA.
*Present address: School of Physics and Astronomy, University of Southampton, Southampton, UK. †**Corresponding author. E-mail: r.c.fear@soton.ac.uk**

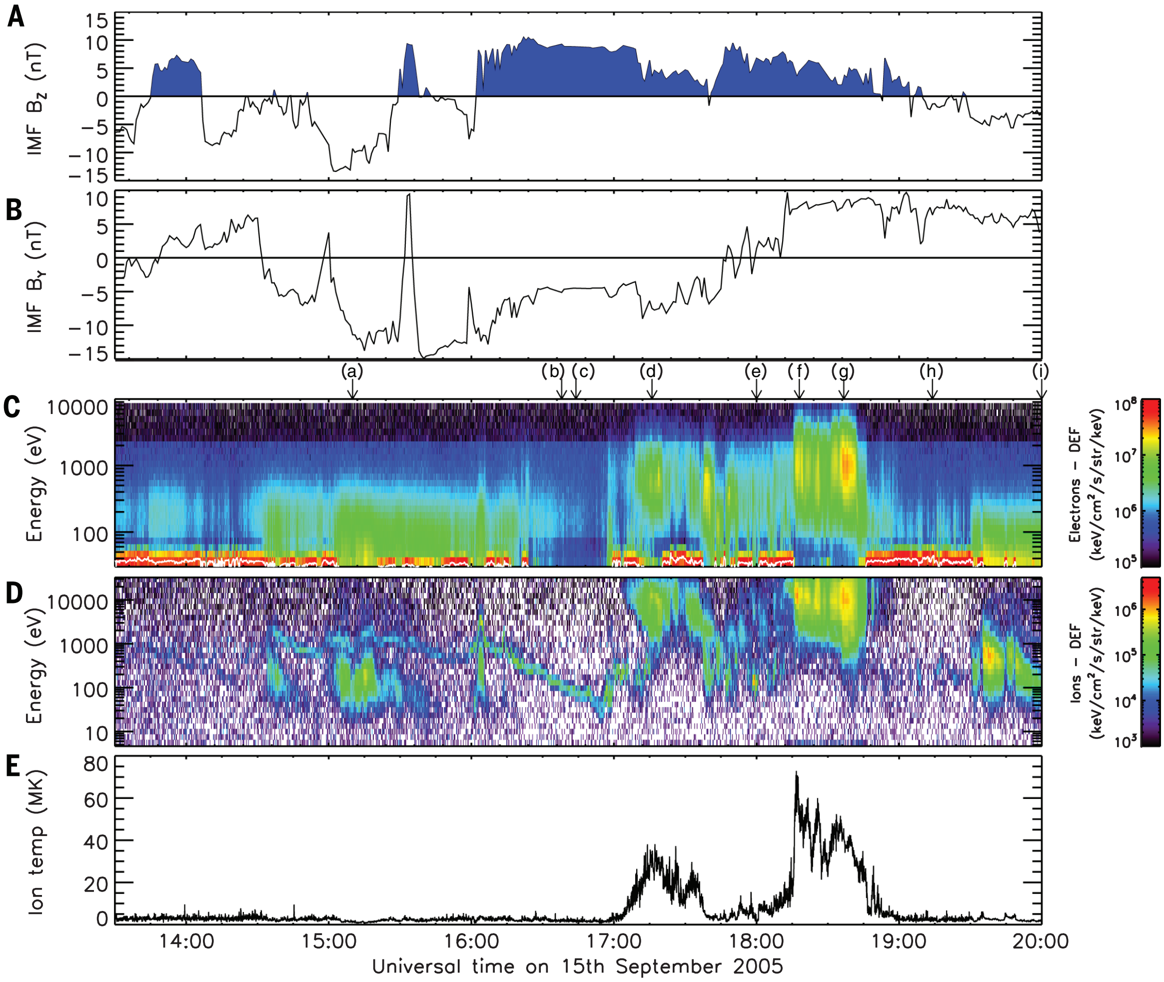

Fig. 2. Time series of the interplanetary and magnetospheric conditions. The top two panels show the simultaneous (**A**) north-south and (**B**) dawn-dusk components of the IMF (B_Z and B_Y, respectively) obtained from the OMNI data set (*25*). The next two panels show the (**C**) electron and (**D**) ion populations observed by Cluster 1 in the magnetotail lobes by the PEACE (*26*) and CIS-HIA (*27*) instruments, respectively. Both panels contain the differential energy flux (DEF) of the electron or ion population plotted as a function of energy and time. The bottom panel (**E**) shows the observed ion temperature. Arrows labeled with lowercase letters (a) to (i) indicate selected times of interest.

proposed (*5*, *6*). Although the link with transpolar arcs has previously been suggested (*6*), the confirmation of the magnetic field topology provides strong evidence that both transpolar arcs and atypically hot lobe plasma observed during periods of northward IMF are caused by the process of magnetic reconnection in the magnetotail, where newly closed lobe flux becomes trapped in the lobe (*10*). Although other proposed mechanisms could explain the closed nature of the magnetic flux threading the transpolar arc, we are not aware of an alternative mechanism that could explain all of the following points: (i) the observation of the lobe immediately before and after the passage of the arc, (ii) the observed back-and-forth motion of the arc, and (iii) the absence of a change in sign of the IMF B_Y (dawn-dusk) component in the hour before the arc formed (see supplementary text). The reconnection mechanism (*10*) predicts that closed magnetic flux observed at high latitudes should be similar in most respects to the plasma sheet, because both contain plasma that was originally contained in the lobe but that has since been heated as a result of the contraction of the field lines after their closure. Our observations confirm that the plasma observed at high latitudes is indeed similar to that observed in the plasma sheet. The net effect of this process is an increase

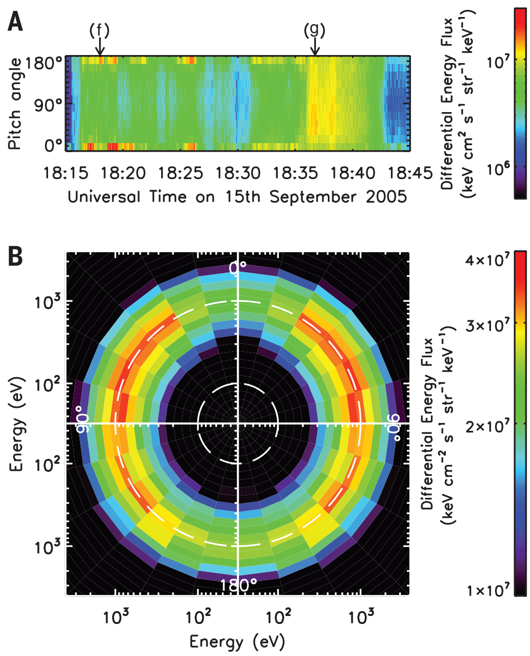

Fig. 3. Electron pitch angle distributions from the hot plasma population. (**A**) Pitch angle distribution of electrons observed above 100 eV between 18:15 and 18:45 UT. (**B**) Electron distribution observed at the time of the highest differential energy fluxes observed by Cluster [corresponding to arrow (g) in Fig. 2; also indicated in Fig. 3A]. The distribution has been computed from five consecutive spacecraft spin periods, centered on time (g), and the color scale has been chosen to emphasize the differences in the field-aligned and perpendicular directions.

in the closed fraction of the magnetotail in one narrow local time sector. An interesting consequence is that as this transpolar arc spans the entire polar cap, the magnetotail is entirely closed in a narrow sector of local time, which highlights the intriguing topology that the

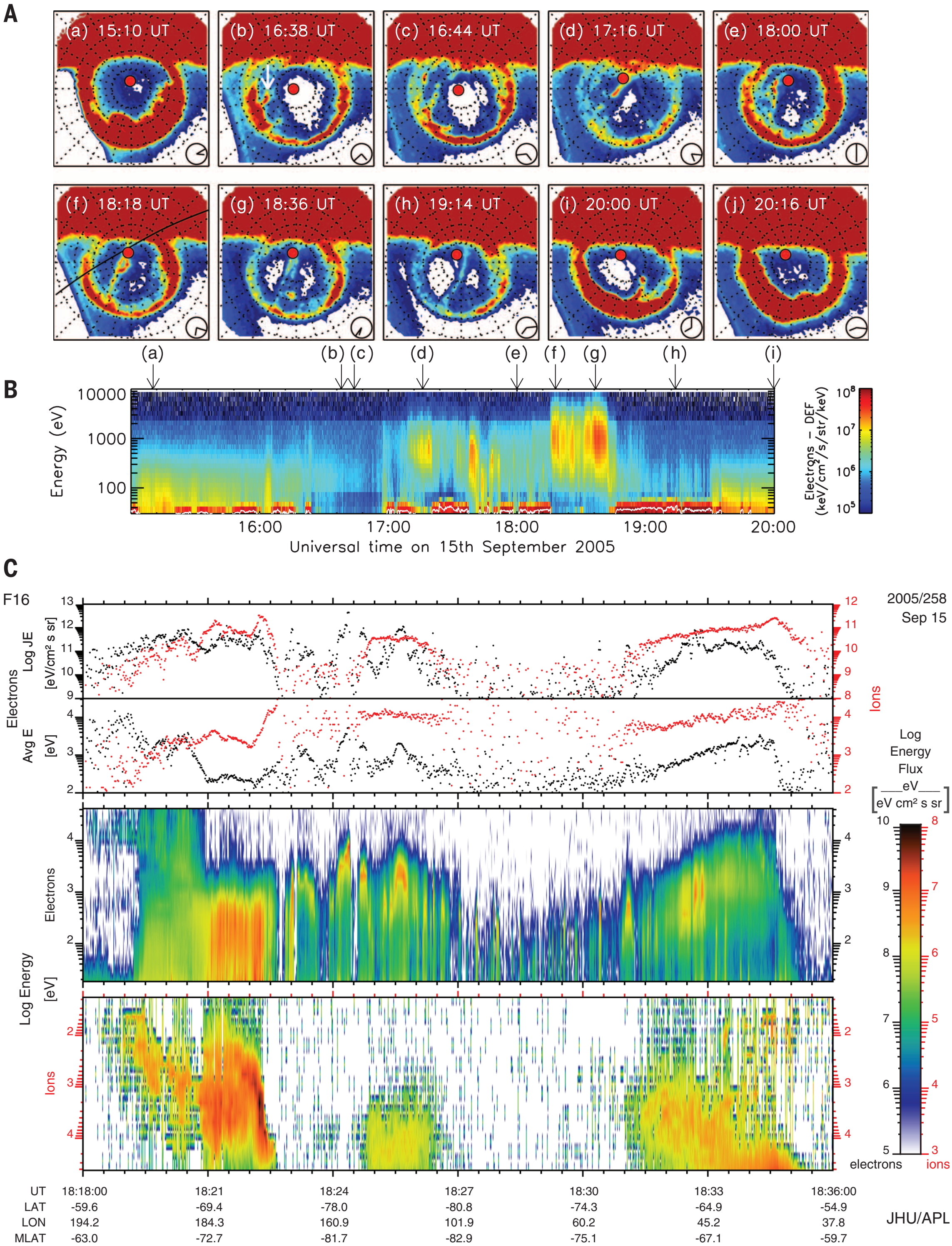

Fig. 4. Summary of the relationship between the auroral and in situ (high- and low-altitude) plasma observations. (**A**) Montage of the auroral observations made by the IMAGE FUV Wideband Imaging Camera on 15 September 2005. Each image has been projected onto a grid of magnetic latitude against magnetic local time with local noon at the top and dawn to the right. Panels (a) to (j) show the transpolar arc [indicated by the white arrow in (b)] at different stages of its evolution, with the footprint of the Cluster spacecraft indicated by a red dot. The times corresponding to panels (a) to (i) are also indicated in Fig. 2 and (B) of this figure. At 15:10 UT (a), the aurora conformed to the standard oval configuration, and the Cluster 1 footprint was in the dim region poleward of the main auroral oval (the polar cap), consistent with the location of the spacecraft in the lobe. At 16:38 UT (b), a small feature emerged from the nightside oval (indicated by the white arrow) and subsequently grew into a transpolar arc [(c) to (i)]. The growth and evolution of the arc [(b) to (h)] occurred while the IMF was northward (Fig. 2A). The arc was initially duskward of the footprint of Cluster [(b) and (c)]. At 17:16 UT (d), the arc intersected the spacecraft footprint before retreating duskward again (e); a subsequent and final period of dawnward motion caused the arc to intersect the spacecraft footprint once more [(f) and (g)] and then move past the spacecraft footprint [(h) and (i)]. After the IMF turned southward at 19:10 UT, the arc retreated to the night side of the polar cap (i) and subsequently disappeared (j). (**B**) Electron population observed by Cluster (replotted from Fig. 2C), with labels showing the times corresponding to (a) to (i). There is an excellent correspondence between the times that the uncharacteristic plasma is observed and the times when the transpolar arc intersected the spacecraft footprint [(d), (f), and (g)]. (**C**) Spectrograms of the electron and ion populations observed by the Defense Meteorological Satellite Program (DMSP) F16 satellite at low altitude during a polar cap crossing made between (f) and (g). Ion precipitation was observed between 18:25 and 18:27 UT, which coincides with the time that the DMSP F16 satellite traversed the arc. [The orbit of the DMSP spacecraft is shown in panel (f) of (A).] The ion and electron precipitation observed at this time is comparable in energy with that observed above the main oval (*7*, *9*) and at high altitudes by Cluster 1 (Fig. 2, C and D), although the electron precipitation observed by DMSP shows signs of further acceleration (inverted "Vs"). In these respects, the precipitation observed by DMSP is typical for transpolar arcs (*18*). Electron precipitation is observed elsewhere in the polar cap and may be associated with fainter polar cap arcs, presumably on open magnetic field lines.

magnetosphere can attain when the IMF points northward.

REFERENCES AND NOTES

1. J. W. Dungey, *Phys. Rev. Lett.* **6**, 47–48 (1961).
2. J. W. Dungey, in *Geophysics: The Earth's Environment*, C. DeWitt, J. Hieblot, A. Lebeau, Eds. (Gordon and Breach, New York, 1963), pp. 505–550.
3. J. D. Menietti, J. L. Burch, *J. Geophys. Res.* **92**, 7503–7518 (1987).
4. Q. Q. Shi *et al.*, *Nat. Commun.* **4**, 1466 (2013).
5. C. Y. Huang *et al.*, *J. Geophys. Res.* **92**, 2349–2363 (1987).
6. C. Y. Huang, J. D. Craven, L. A. Frank, *J. Geophys. Res.* **94**, 10137–10143 (1989).
7. L. A. Frank, J. D. Craven, J. L. Burch, J. D. Winningham, *Geophys. Res. Lett.* **9**, 1001–1004 (1982).
8. L. A. Frank *et al.*, *J. Geophys. Res.* **91**, 3177–3224 (1986).
9. W. K. Peterson, E. G. Shelley, *J. Geophys. Res.* **89**, 6729–6736 (1984).
10. S. E. Milan, B. Hubert, A. Grocott, *J. Geophys. Res.* **110**, A01212 (2005).
11. D. A. Hardy, W. J. Burke, M. S. Gussenhoven, *J. Geophys. Res.* **87**, 2413–2430 (1982).
12. M. S. Gussenhoven, E. G. Mullen, *J. Geophys. Res.* **94**, 17121–17132 (1989).
13. N. Østgaard, S. B. Mende, H. U. Frey, L. A. Frank, J. B. Sigwarth, *Geophys. Res. Lett.* **30**, 2125 (2003).
14. R. C. Fear, S. E. Milan, *J. Geophys. Res.* **117**, A03213 (2012).
15. A. Kullen, M. Brittnacher, J. A. Cumnock, L. G. Blomberg, *J. Geophys. Res.* **107**, 1362 (2002).
16. N. Østgaard *et al.*, *J. Atmos. Sol. Terr. Phys.* **69**, 249–255 (2007).
17. A. Goudarzi, M. Lester, S. E. Milan, H. U. Frey, *Ann. Geophys.* **26**, 201–210 (2008).
18. J. A. Cumnock *et al.*, *J. Geophys. Res.* **116**, A02218 (2011).
19. A. Kullen, in *Auroral Phenomenology and Magnetospheric Processes: Earth and Other Planets*, A. Keiling, E. Donovan, F. Bagenal, T. Karlsson, Eds. (Geophysical Monograph 197, American Geophysical Union, Washington, DC, 2012), pp. 69–80.
20. R. C. Fear, S. E. Milan, *J. Geophys. Res.* **117**, A09230 (2012).
21. A. P. Walsh *et al.*, *J. Geophys. Res.* **118**, 6042–6054 (2013).
22. S. B. Mende *et al.*, *Space Sci. Rev.* **91**, 271–285 (2000).
23. N. A. Tsyganenko, in *Proceedings of the Third International Conference on Substorms (ICS-3)*, Versailles, France, 12 to 17 May 1996 (SP 389, European Space Agency, Noordwijk, Netherlands, 1996), pp. 181–185.
24. C. T. Russell, *Cosmic Electrodyn.* **2**, 184–196 (1971).
25. J. H. King, N. E. Papitashvili, *J. Geophys. Res.* **110**, A02104 (2005).
26. A. N. Fazakerley *et al.*, in *The Cluster Active Archive - Studying the Earth's Space Plasma Environment*, H. Laakso, M. Taylor, P. Escoubet, Eds. (Springer, Dordrecht, Netherlands, 2010), pp. 129–144.
27. H. Rème *et al.*, *Ann. Geophys.* **19**, 1303–1354 (2001).

ACKNOWLEDGMENTS

Work in the UK was supported by Science and Technology Facilities Council (STFC) Ernest Rutherford Fellowship ST/K004298/1 and STFC grants ST/K001000/1 and ST/K000977/1. R.M. is supported by the Belgian Science Policy Office through the Solar-Terrestrial Center of Excellence. French participation in the Cluster project is funded by the Centre National d'Etudes Spatiales (CNES). IMAGE satellite work at the University of California, Berkeley, was supported through a Southwest Research Institute subcontract under NASA contract NAS5-96020. We acknowledge support from the International Space Science Institute through funding of its International Team on Polar Cap Arcs, and we are grateful for discussions with members of the team. Cluster data were obtained from the Cluster Active Archive (http://caa.estec.esa.int/caa/), and the IMAGE FUV data were provided by the NASA Space Science Data Center (http://nssdc.gsfc.nasa.gov/space/). The OMNI IMF data were obtained through NASA's CDAWeb (http://cdaweb.gsfc.nasa.gov/), for which we acknowledge J. H. King, N. Papatashvilli, and the principal investigators of the magnetic field and plasma instruments on the Geotail and Advanced Composition Explorer (ACE) spacecraft. The DMSP particle detectors were designed by D. Hardy of Air Force Research Laboratory, and data were obtained from the Johns Hopkins University Applied Physics Laboratory.

SUPPLEMENTARY MATERIALS

www.sciencemag.org/content/346/6216/1506/suppl/DC1
Supplementary Text
Fig. S1
References (*28–38*)
Movie S1

12 June 2014; accepted 19 November 2014
10.1126/science.1257377

BIOPHYSICS

Extreme electric fields power catalysis in the active site of ketosteroid isomerase

Stephen D. Fried,* Sayan Bagchi,† Steven G. Boxer‡

Enzymes use protein architecture to impose specific electrostatic fields onto their bound substrates, but the magnitude and catalytic effect of these electric fields have proven difficult to quantify with standard experimental approaches. Using vibrational Stark effect spectroscopy, we found that the active site of the enzyme ketosteroid isomerase (KSI) exerts an extremely large electric field onto the C=O chemical bond that undergoes a charge rearrangement in KSI's rate-determining step. Moreover, we found that the magnitude of the electric field exerted by the active site strongly correlates with the enzyme's catalytic rate enhancement, enabling us to quantify the fraction of the catalytic effect that is electrostatic in origin. The measurements described here may help explain the role of electrostatics in many other enzymes and biomolecular systems.

Ketosteroid isomerase (KSI) is a small, proficient enzyme with one of the highest known unimolecular rate constants in biochemistry (*1*, *2*), which has prompted extensive study of its mechanism and the catalytic strategies it uses (*3–5*). In steroid biosynthesis and degradation, KSI alters the position of a C=C double bond (Fig. 1A) by first abstracting a nearby α proton (E•S ⇌ E•I), forming a charged enolate intermediate (E•I), and then reinserting the proton onto the steroid two carbons away (E•I ⇌ E•P). The removal of a proton in the first step initiates a rehybridization that converts the adjacent ketone group to a charged enolate, an unstable species that is normally high in free energy and so slow to form. The reaction is therefore expected to produce an increase in dipole moment at the carbonyl bond ($|\Delta\vec{\mu}_{rxn}|$), suggesting that KSI may facilitate this reaction by exerting an electric field ($\vec{F}_{enz}$) on this bond that stabilizes it in the intermediate form and the preceding transition state (Fig. 1B). Using vibrational Stark effects, we have measured the electric field that KSI exerts on this C=O bond, providing quantitative experimental evidence for the connection between electrostatics and catalytic proficiency.

The frequencies of certain vibrations (such as the C=O stretch) shift in a linear manner with the electric field experienced by that vibration from its environment, a phenomenon known as the linear vibrational Stark effect (*6*, *7*). Through this effect, we have shown that vibrations can be used as probes of local electrostatic fields. The nitrile group has been widely deployed to measure electric fields inside enzymes and their relationship to mutation (*8*), ligand occupancy (*9*), or conformational changes over the catalytic cycle (*10*). In this study, we have focused on the C=O group of the inhibitor 19-nortestosterone (19-NT) (Fig. 1C), because when 19-NT binds, the C=O group is loaded directly into the catalytic machinery (*11*, *12*). In this way, 19-NT's C=O vibrational (infrared) frequency shift probes the electrostatic environment that the substrate's C=O bond would experience in the active site, except 19-NT cannot react due to the position of the C=C bond.

To calibrate the sensitivity of 19-NT's C=O vibrational frequency to an electric field, we used two complementary approaches. In Stark spectroscopy (Fig. 2, A and B), an external electric field of known magnitude is applied to a frozen glass containing 19-NT, and the accompanying effect on the vibrational spectrum is recorded (*7*). By fitting the Stark spectrum (Fig. 2B) to derivatives of the absorption spectrum (Fig. 2A), the vibration's difference dipole can be extracted: $|\Delta\vec{\mu}_{C=O}|f = 1.39 \pm 0.05$ cm^{-1}/(MV/cm), where f is the local field factor (fig. S1) (*6*, *7*, *13*). A vibration's difference dipole is its linear Stark tuning rate; that is, 19-NT's C=O vibrational frequency shifts ~$1.4/f$ cm^{-1} for every MV/cm of electric field projected onto the C=O bond axis, whether the source of that field is an external voltage (as in Stark spectroscopy) or an organized environment created by an enzyme active site ($\vec{F}_{enz}$) that we wish to characterize. Whenever an external field is applied to a vitreous sample, vibrational bands will broaden because 19-NT molecules (and their C=O bonds) are randomly oriented with respect to the fixed direction of the external electric field (*6*, *7*). By contrast, a vibrational probe will have a fixed orientation with respect to a protein electric field when bound to a protein, and as such the linear Stark effect then produces spectral shifts instead of broadening. The C=O vibration's Stark tuning rate does not appreciably change when C=O accepts a hydrogen bond (fig. S2), implying that the frequency still responds to fields linearly even when C=O participates in stronger interactions, although those interactions themselves are associated with larger electric fields (*14*).

Department of Chemistry, Stanford University, Stanford, CA 94305-1052, USA.
*Present address: Protein and Nucleic Acid Chemistry Division, Medical Research Council Laboratory of Molecular Biology, Cambridge CB2 0QH, UK. †Present address: Physical and Materials Chemistry Division, National Chemical Laboratory (CSIR), Pune 411008, India.
‡Corresponding author. E-mail: sboxer@stanford.edu